

Fabrication, Flow Assembly, and Permeation of Microscopic Any-Shape Particles

Arne Lüken, Lucas Stüwe, Sebastian Bernhard Rauer, Jesco Oelker, John Linkhorst, and Matthias Wessling*

Today, millimeter-sized nonspherical any-shape particles serve as flexible, functional scaffold material in chemical and biochemical reactors tailoring their hydrodynamic properties and active surface-to-volume ratio based on the particle's shape. Decreasing the particle size to smaller than 100 μm would be desired as it increases the surface-to-volume ratio and promotes a particle assembly based on surface interactions, allowing the creation of tailored self-assembling 3D scaffolds. This study demonstrates a continuous high-throughput fabrication of microscopic 3D particles with complex shape and sub-micron resolution using continuous two-photon vertical flow lithography. Evolving from there, in-channel particle fabrication into a confined microfluidic chamber with a resting fluid enables the precise fabrication of a defined number of particles. 3D assemblies with various particle shapes are fabricated and analyzed regarding their permeability and morphology, representing convective accessibility of the assembly's porosity. Differently shaped particles highlight the importance of contact area regarding particle–particle interactions and the respective hydraulic resistance of an assembly. Finally, cell culture experiments show manifold cell–particle interactions promising applicability as bio-hybrid tissue. This study pushes the research boundaries of adaptive, responsive, and permeable 3D scaffolds and granular media by demonstrating a high throughput fabrication solution and a precise hydrodynamic analysis method for micro-particle assemblies.

required for bioreactors enabling immobilizing enzymes, cells or microorganisms on the surface of the reactor's internal packing. Such internal packings are scalable and in fact allow transferring batch toward continuous processes.^[1] The biochemical reaction is performed in living cells on the surface or catalyzed by the immobilized enzyme on the surface, making the surface to volume ratio the main factor affecting the process efficiency.^[2] Hollow fiber membrane bioreactors^[3,4] and packed-bed bioreactors^[5] both show high surface to volume ratios and are therefore the two established reactor types in industrial processes. Key to the performance of such packed-bed reactors is tuning the properties of the particles that define the desired reactor characteristics. These particles' properties range from the material with a specific surface charge, softness, or rigidity to the macroscopic structure with particular particle size, shape, and desired surface roughness.^[6] They affect the biological environment, including the adhesion and development of cells, and the engineering performance indicators, such as the hydraulic resistance,

the packing density, and the surface to volume ratio. For example, the particle softness affects the cells adhesion^[7] as well as the flow-dependent compressibility of the packed bed, which increases the pressure loss.

The influence of particle shape on pressure drop, permeability, and active catalyst surface is also applied on a larger scale at fixed bed reactors for particle sizes of several centimeters. By tailoring particle shapes, from spherical to cylindrical, tubular or more complex-shaped particles, the hydrodynamic pressure drop and the active surface area are tailored for the specific application in experiments^[8] as well as in simulation.^[9] Such irregular assemblies of porous any-shape particles are a promising alternative to applications of periodic open cellular structures (POCS) as a fixed bed. The POCS geometry allows predicting and tailoring of the hydrodynamic properties, including the pressure drop.^[10,11] However, tailoring any-shape particle assemblies' porosity and pressure drop holds great benefits regarding automated fabrication, process adjustment, and installation.


For bioprocessing and tissue engineering applications, assemblies made from double-digit micrometer-sized particle

1. Introduction

Constructing percolating interconnected internal surface is a prerequisite for surface controlled reactions as for instance

A. Lüken, L. Stüwe, S. B. Rauer, J. Oelker, J. Linkhorst, M. Wessling
Chemical Process Engineering
RWTH Aachen University
Forckenbeckstr. 51, Aachen 52074, Germany
E-mail: manuscripts.cvt@avt.rwth-aachen.de

M. Wessling
DWI - Leibniz Institute for Interactive Materials
Forckenbeckstr. 50, Aachen 52074, Germany

 The ORCID identification number(s) for the author(s) of this article can be found under <https://doi.org/10.1002/sml.202107508>.

© 2022 The Authors. Small published by Wiley-VCH GmbH. This is an open access article under the terms of the Creative Commons Attribution-NonCommercial-NoDerivs License, which permits use and distribution in any medium, provided the original work is properly cited, the use is non-commercial and no modifications or adaptations are made.

DOI: 10.1002/sml.202107508

building blocks enhance the surface-to-volume ratio and allow cells to interact with the geometrical structures of similar-sized objects. Several fabrication techniques are applied in research to fabricate such complex-shape micro-particles and can be structured in batch fabrication, horizontal-flow lithography, and vertical-flow lithography. Batch fabrication includes molding techniques for rods^[12,13] and 3D printing of complex 3D particles on a static substrate using two-photon polymerization.^[14] These batch techniques are not suited for continuous fabrication and are therefore hardly scalable. Microfluidic horizontal-flow lithography enables the fabrication of anisometric particles by exposing light perpendicularly into a photo-resin-filled channel. For example, rod-shaped particles can be fabricated by centering the photo resin by a jet and pulsating a spotlight source.^[15] More complex 2.5D particles can be fabricated by projecting photo-masked-shaped parallel light into a channel, which is filled with the liquid photo-resin so that particles are formed in the shape of the light beam, and the height of the channel.^[16] This technique is applied for various materials^[17] and flow interruption during particle formation improves its resolution.^[18] In addition, high-resolution two-photon polymerization can be applied in a horizontal flow for the fabrication of 3D particles by correcting the laser pathway in flow-direction depending on the print-time.^[19] Rotating the illumination direction parallel to the fluid flow results in vertical flow lithography, which was implemented with a stop-flow set-up using UV-projection.^[20] However, high-resolution in-flow printing is only possible by moving the polymerization level away from the channel walls inside the center of the laminar flow profile. Lölsberg et al. suggested this technique by applying two-photon polymerization in the vertical flow and fabricating high-resolution micro-tubular structures with sub-micron-sized porosity.^[21]

In today's state-of-the-art particle fabrication technologies, the production of any-shape micro particles in a reasonable size range for bioprocessing and tissue engineering applications is limited regarding 3D complexity, resolution, and throughput. Therefore, the analysis of micro-particle assemblies are to date limited to spherical rigid and soft particles.^[22–25] The morphology of an assembly depends strongly on its formation process, which results from particle interactions, extensively studied for nano-particle self-assembly within the last 30 years.^[26] All the progress in nano-particle assembly ranging from molecular synthesis to controlled 1D, 2D, and 3D arrangement, emerges in assemblies with tremendous precision by considering all material properties including composition, crystal structure, surface chemistry, and morphology. However, nano-particle self-assemblies are restricted to a few tens of micrometers.^[26,27] Accomplishing technical applications requires larger micron-scale building blocks by transferring molecular synthesis routes and nano-particle properties to 3D micro-particle fabrication and functionalization. The micro-particle's shape determines the particle-contact points and thereby activates the interaction of particles depending on their properties, including charge, softness, and solvent wettability.^[28,29] This will potentially enable a layer-by-layer in-flow particle self assembly creating a 3D-structure (Figure 1) similar to the various applications in layer-by-layer assemblies of nanoparticles and macromolecules.^[30] The roadmap toward a controlled macroscopic 3D-assembly opens many questions regarding the

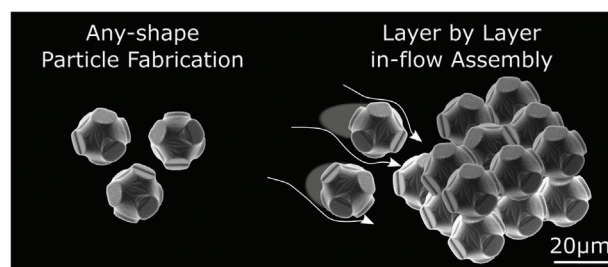


Figure 1. Tailoring micro-particle's shape by novel fabrication methods empowers a new roadmap toward creating self-assembled layer-by-layer in-flow assemblies, as envisioned in this assembly collage of single particle SEM micrographs. Applied as tissue, the particle shape and material would tailor the assembly's stability and its hydraulic resistance for nutrient supply.

assembly process^[26] and the assembly's behavior upon application of forces, such as permeation or the interaction of cells with the self-assembled bio-hybrid tissues.

This study applies the vertical flow two-photon lithography (VFL) technology^[21] in a continuous process for fabricating complex 3D shaped particles (Figure 1a) from different materials. These particles are inflow self assembled in microfluidic channels as 3D scaffold and the scaffolds' hydraulic resistances and packing densities are analyzed via permeation experiments. Engineering the particle's 3D shape permits a description of the assemblies' hydraulic resistances depending on particle shape, size and material. Finally, a first application as cell tissue discloses biocompatibility and manifold cell-particle interactions.

2. Results and Discussion

2.1. Continuous Vertical Flow Any-Shape Particle Fabrication

3D any-shaped particles with 20 μm diameter are synthesized continuously using a VFL process. The channel design of Lölsberg et al.^[21] enables 3D any-shape particle synthesis by moving a two-photon laser in a single xy -plane while the flow transports the printed xy -slice continuously in the z -direction (Figure 2a,b). The print time of each xy -slice is adapted to the flow rate by adding a wait command depending on the trajectory length of the laser path using a python script (Figure S1, Supporting Information). This script additionally removes all z -movement commands from the print file, so that Nanoscribe's "Describe" software can be used to slice complex geometries.

The printing layer inside the outlet channel is located 200 μm above the glass slide and is limited by the objective's focal distance. The channel design promotes a laminar flow profile with parallel streamlines at the printing level. However, the particles' shape unravels a nonuniform flow depending on the print position. We printed cubes in the centered symmetry axes of the outlet channel ($r = 0 \mu\text{m}$), at two positions further discentered from the symmetry axes at a radial distance of 82 and 165 μm and analyzed their height-to-width ratio as well as their distortion angle α (Figure 2d,e). Particles printed in the center of the channel show the desired height-to-width ratio and distortion angle α of 90°, while the discentered particles show undesired geometry (Figure 2 d1–d3). The shifted distortion angle α can

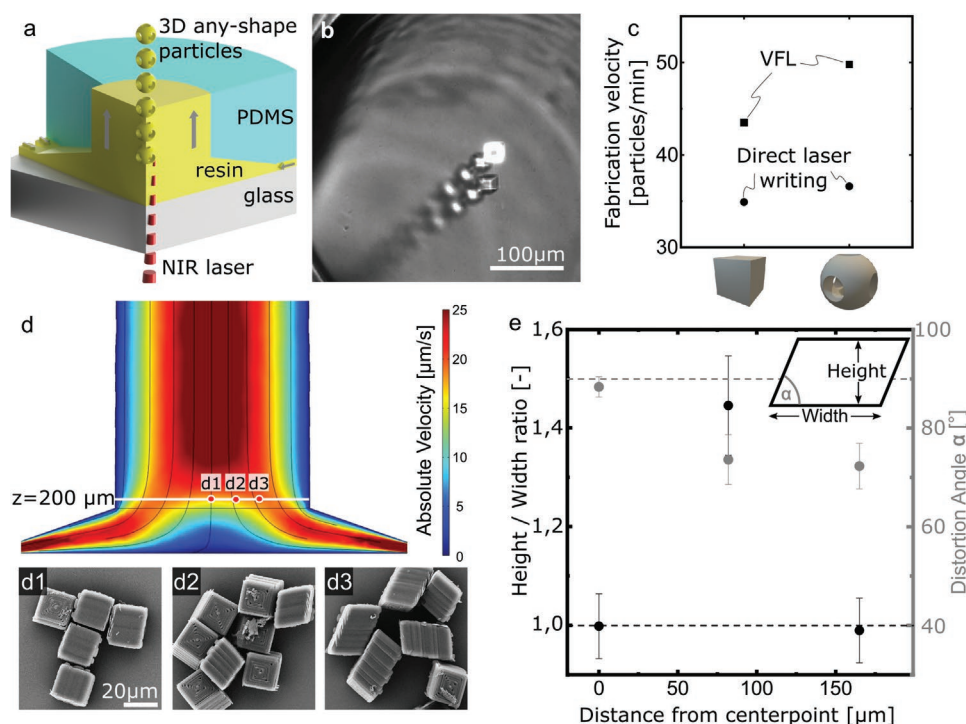


Figure 2. Continuous VFL particle synthesis. a) Visual representation of the fabrication process. b) Micrograph of the continuous fabrication process with particles printed one after the other in a zigzag pattern. c) Comparison of the fabrication velocity of VFL with traditional two-photon lithography. d) Cross-section of a 3D computational fluid dynamics (CFD) simulation of the flow field and micrographs of the particles, depending on the print position ((d1) at $r = 0 \mu\text{m}$, (d2) at $r = 82 \mu\text{m}$, (d3) at $r = 165 \mu\text{m}$). e) Analysis of the particles' shape at different print positions.

be correlated to nonparallel streamlines in the print layer as a result of an undeveloped laminar flow profile and suits well to CFD simulations (Figure 2d). The increased height-to-width ratio of the particles printed at a radius of $82 \mu\text{m}$ is also a result of the undeveloped laminar flow profile with a ring-shaped velocity profile at the beginning of the outlet channel. The CFD simulations phenomenologically confirm the ring-shaped profile at the print position (Figure 2d). Still, the relative flow velocities at the three printing positions do not match the measured particle height-to-width ratio. Hence, a precise height-to-width ratio was achieved using an iterative fabrication process with subsequent size analysis using a microscope.

Additionally, we evaluated the fabrication velocity of the VFL in comparison to traditional two-photon direct laser writing on a substrate applying the same processing parameters. The particles in VFL were printed one after each other at two offset positions (Figure 2b) with an x/y -distance of $20 \mu\text{m}$ to prevent the particles from adhering to one another. Thus, the particles could be printed directly one after the other, with no waiting time between two particles. Additionally, the VFL does not perform z -movement of the stage between the printed layers, so that the printing time per single particle also decreases. Both effects result in an accelerated fabrication velocity of VFL (Figure 2c) in comparison to two-photon direct laser writing on a substrate. However, the accelerated fabrication of VFL in comparison to traditional direct laser writing depends on the geometry of the printed structure. In VFL, each printed layer must last the same duration because the flow velocity is constant. Wait commands compensate trajectory length variations per

layer. Accordingly, structures with a similar trajectory length per layer achieve the greatest time-wise benefit. The final absolute speeds depend on the particle's size, its uniformity, the surface roughness, and the overall printed volume.

The VFL process prints the particles as a rigid structure, polymerizing the complete inner volume of the printed particles. However, as known for other two-photon polymerization processes, the process parameters, including the laser power, the writing speed, and the hatching distance, influence the degree of conversion and the respective material properties significantly.^[31,32] Therefore, the fabrication parameters for this study were chosen with hatching and slicing distance ($x/y = 0.3 \mu\text{m}$, $z = 0.6 \mu\text{m}$) significantly smaller than the voxel diameters ($x/y = 0.6 \mu\text{m}$, $z = 3 \mu\text{m}$) with a high laser power applied (100%, 50 mW). These processing parameters with mainly overlapping voxels result in a high degree of conversion and symmetric material properties in all three dimensions.^[31] However, the elliptical shape of the two-photon polymerization voxel results in slight deviations of the surface roughness of the particles (Figure 2 d1,d3). This surface resolution can be increased by decreasing the hatching and slicing distance, which, just like any other two-photon polymerization process, will increase the printing time.

Using VFL, 3D particles were fabricated continuously by printing for 72 h resulting in more than 150 000 particles. This proof of principle showcases the potential of the automated, continuous, and scalable particle fabrication technology toward a high throughput production of 3D structures and discloses micron-sized any-shape structures to the next level of potential

applications. Though, the technological limitations of direct laser writing also present in the VFL process, the overall throughput mainly depends on the fabricated volume, resulting in a tradeoff between resolution and sample size. Smaller objective magnifications reduce the printing time by increasing the voxel volume but simultaneously reduce the resolution and vice versa. Direct laser writing VFL is therefore advantageous for high-resolution micron-scale particles. Technology transfer to larger structures and higher fabrication rates requires increased energy input, increased scan speeds, and adaptive voxel sizes. Based on the small channel diameters, the flow rate is highly laminar ($Re < 1$) and does not limit the process even if up-scaled for larger structures.

2.2. Hydraulic Resistance of Any-Shape Particle Assemblies

2.2.1. Microfluidic Trapping of Any-Shape Particles

In a scaffold applications, perfusion of cell-covered tissues accelerates nutrient and oxygen supply compared to diffusive mass transport. Accordingly, the scaffold's hydrodynamic resistance is of great importance for potential applications. We analyze the hydrodynamic properties of scaffold like any-shape particle assemblies by inserting free-flowing 3D particles inside a microfluidic channel and assembling them on a porous filter structure. These filter structures are located at the inlet and outlet and trap the particles in the observation and analysis domain (Figure 3c). The particles were fabricated directly inside the analysis domain by two-photon printing in a resting fluid (Figure 3b), enabling precise control of particle material, size,

shape, and amount. After the printing process, the remaining liquid resin was removed by flushing developer solvent and afterward filtration fluid through the channel system permeating the assembly (see Experimental Section for details).

For analyzing the particles' influence on the hydraulic resistance of an assembly, we chose three different particle shapes: Spheres ($d = 20\ \mu\text{m}$), porous spheres with $8\ \mu\text{m}$ holes along all axes ($d = 20\ \mu\text{m}$), and P-Schwarz triple periodic minimal surface (TPMS) unit cells ($d = 20\ \mu\text{m}$) (Figure 3a). Additionally, we chose a mixture of polydisperse particles with a pyramid-distributed size range from 10 to $30\ \mu\text{m}$ (details in Figure S4, Supporting Information). We varied the particle's softness by applying a rigid material with a Young's Modulus of $4730\ \text{MPa}$ (IP-L) and a soft material with a Young's Modulus of $15.3\ \text{MPa}$ (IP-PDMS). The $20\ \mu\text{m}$ sized soft spheres with holes squeezed through the filter structure, though, we increased the diameter of the soft particles to $40\ \mu\text{m}$.

2.2.2. Repeatability of Permeation Experiments for Rigid and Soft Particles

The permeation experiments were performed by increasing and subsequently releasing the feed pressure in small steps from 20 to $150\ \text{mbar}$ and measuring the flow permeating the packed bed of particles over three cycles (Figure 4b,e). The assembly was in situ visualized in a brightfield microscope (Figure 4a,d) and the relative compression of the assembly was evaluated by image analysis (Figure 4c,f). Finally, the void fraction of the packing was calculated by combining the exact amount of trapped particles in the analysis domain with the overall assembly volume.

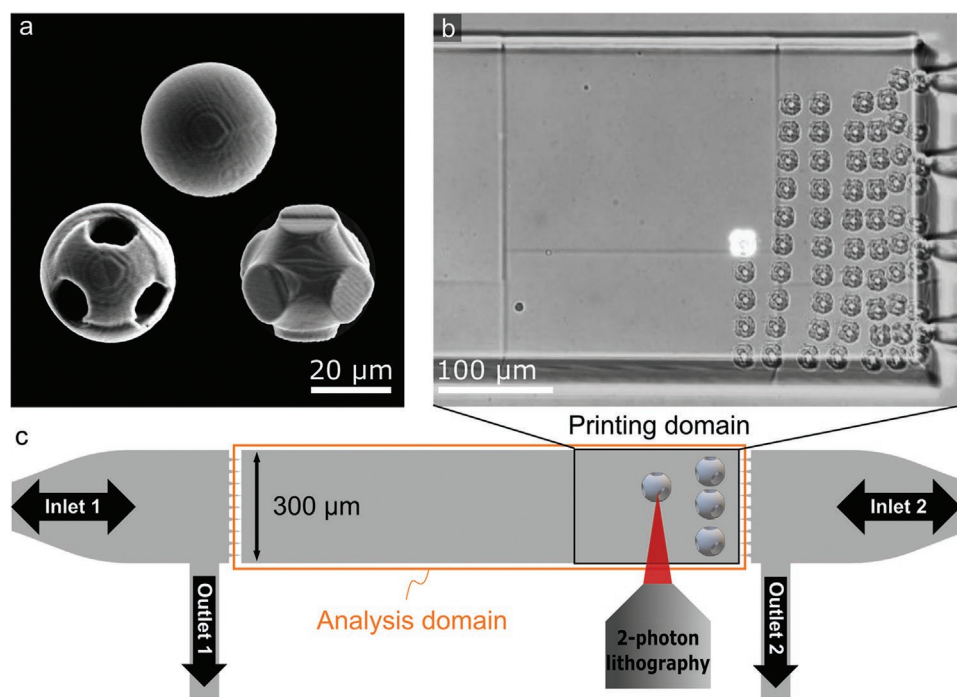


Figure 3. Direct 3D particle in-channel fabrication by a) two-photon printing of any-shape particles b) in a non-moving fluid. (a) shows a collage of single particle SEM micrographs of the different particle shapes investigated in this study. c) The channel design traps the any-shape particles by two filter structures at the inlet and outlet.

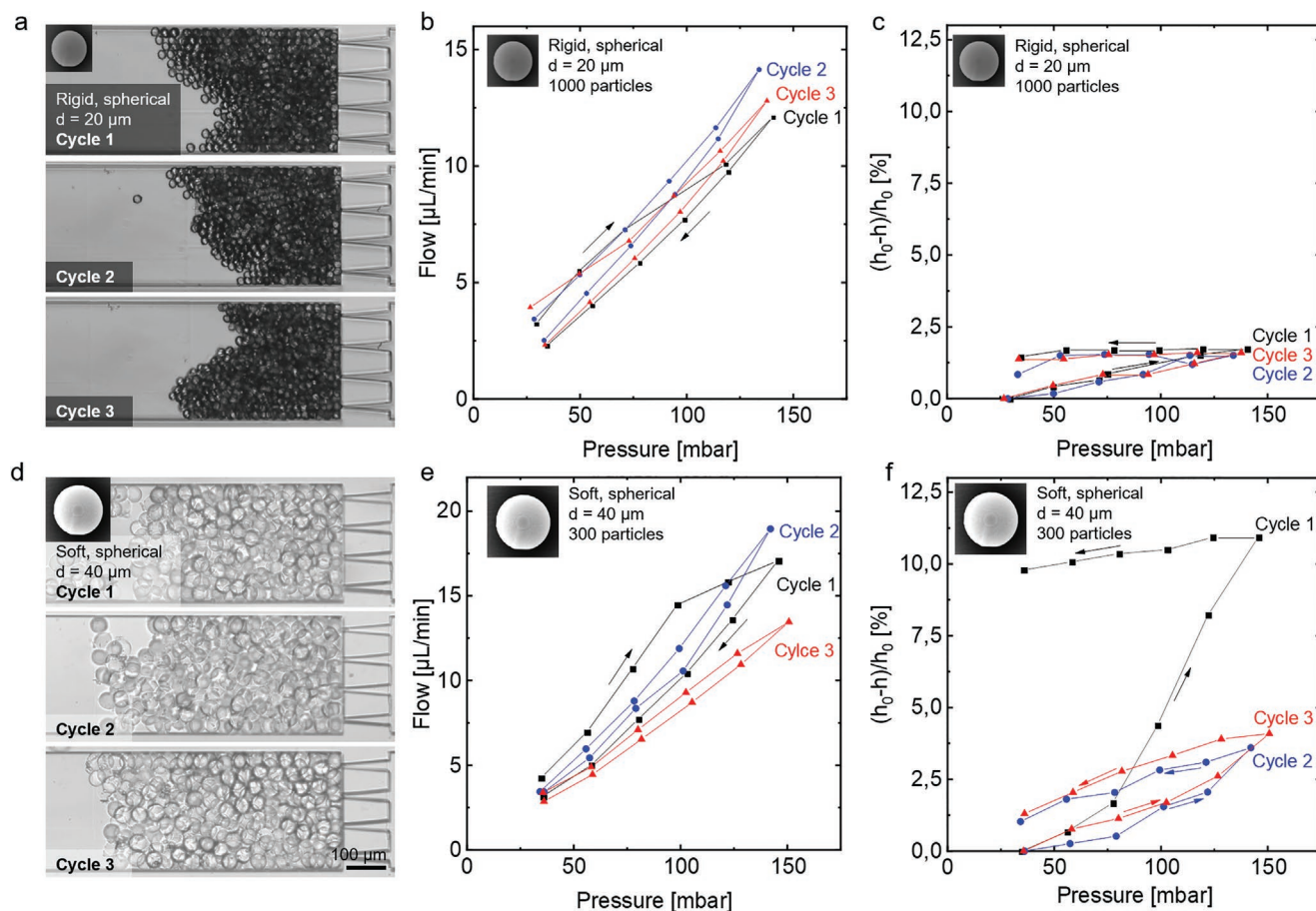


Figure 4. Three permeation cycles with backflushing and ultrasonic treatment in between for a–c) rigid 20 μm sized particles and d–f) soft 40 μm sized particles. Each cycle is analyzed by b,c) the permeating flow at different pressure steps and c,f) the relative compression of the assembly during pressure stepping. The data from the relative compression is taken from the micrographs of each pressure step. a,d) Exemplary micrographs of the assemblies in the highest compression state show that each cycle results in a different morphology.

The trapping of particles between two filter structures enables a repetition of the permeation cycles with the same particles by forward- and backward flushing. With this unique experimental design, we are not only able to accurately determine the particle number and shape but can also optically study the filtration process in situ and couple this to specific resistances of the particle assembly via flux and pressure data. We performed three permeation cycles for each experiment, each with a backflushing and ultrasonication cycle in between, redispersing the particles.

The shape of the rigid assemblies looks different in each cycle, predominantly with thicker assemblies at the channel walls and a thinner assembly in the channel center position (Figure 4a). The assembly's shape depends on the formation process and the particles' location before creating the assembly. The rigid particles made from IP-L resin tend to arrange at the channel surface while being in solution. Therefore, most particles arrive at the filter structure at the top and bottom during the assembly's formation, resulting a v-shape of the assembly (see Figure S7, Supporting Information for the formation process). The soft IP-PDMS particles have a lower tendency to accumulate at the channel wall and therefore create homogeneous assemblies.

The rigid spheres show repeatable flow rates and compression curves during all three cycles (Figure 4a–c). The soft particles show an increased variation in the flow, primarily upon the first permeation cycle. The measured flow is higher during pressure increase (Figure 4e) than during pressure release. The compression curve (Figure 4f) supports the flow measurement by an irreversible relative compression of 10%. Although the flow measurements represent similar results of the second and third permeation cycle (Figure 4d), redispersion was not entirely successful creating agglomerates affecting the assembly's formation process (Figure S5, Supporting Information). Accordingly, the compression curve during re-permeation of soft particles shows mainly the irreversible share of the compression. The similar slope of all three decompression cycles confirms the theory about reversible and irreversible compression, which was similarly reported in microfluidic filtration experiments filtering soft spherical PEG particles.^[33] The phenomenon of a reversible and irreversible hydraulic resistance upon compression of soft matter was also reported for biofilms on membrane surfaces using optical coherence tomography.^[34,35] This study illustrates the difference between hard and soft particles during compression and confirms the importance of particle rigidity upon tailoring reorientations and the inner structure of particle assemblies.

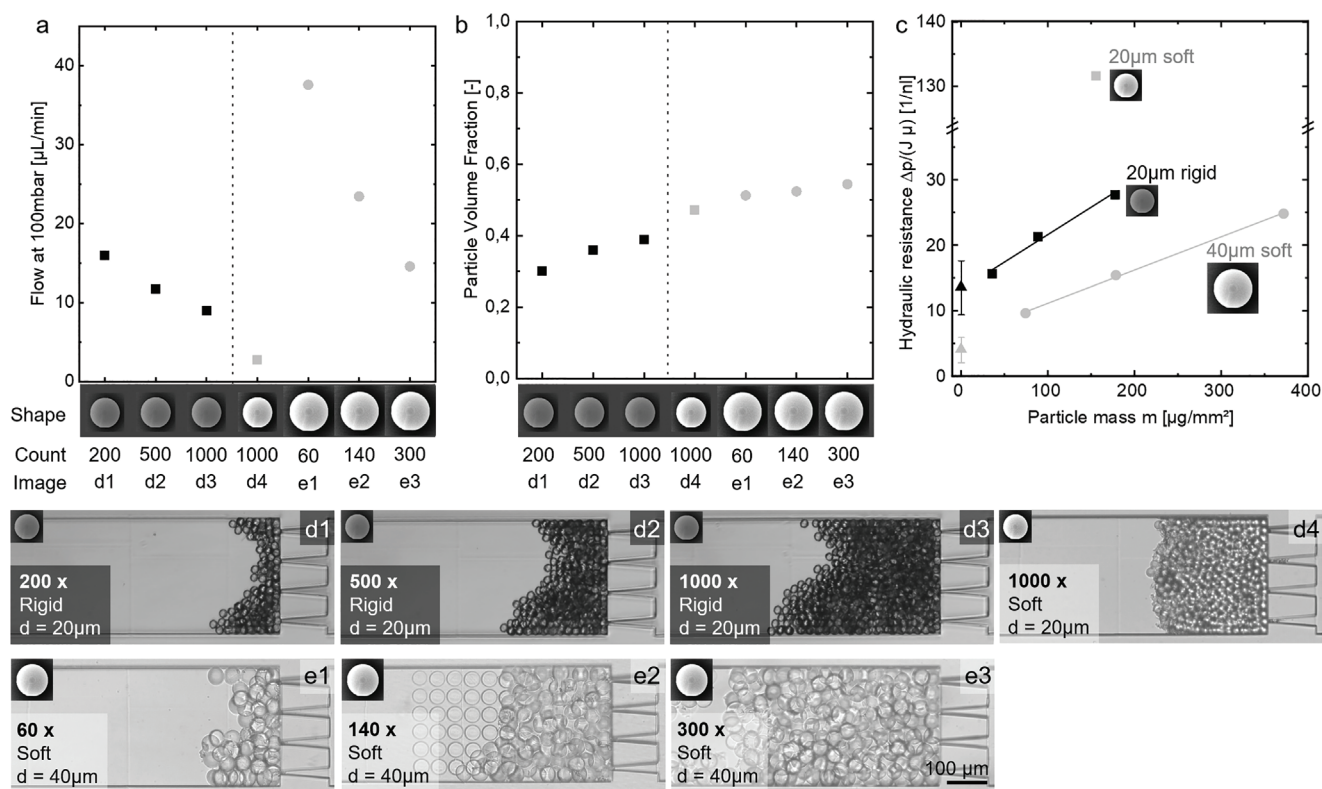


Figure 5. Influence of particle number on a) permeation flow, b) volume fraction, and c) hydraulic resistance for rigid (back) and differently sized soft (gray) particles. The permeating flow (a) is interpolated for a trans-assembly pressure of 100 mbar. The volume fraction (b) is calculated from the micrographs of the corresponding experiments (d) and (e). The particle mass in (c) calculates from the particle number, its diameter and the material density. The interpolation of the three masses represents the linear correlation. The triangles at zero-mass represent the hydraulic resistance of six individually measured empty channel resistances with the respective solvent.

2.2.3. Correlation of the Hydraulic Resistance and Packing Density to the Amount of Particles

The coupled in-chip fabrication and subsequent analysis method, including microfluidic trapping of a well-defined amount of any-shaped particles and filtration procedure, allows the investigation of different particle amounts influencing the hydraulic resistance and the packing density for rigid and soft particles. However, as the assemblies' degree of agglomeration after the first permeation cycle unreproducibly affects the hydraulic resistance of the second and third permeation cycle, we only take the hydraulic resistance of the first pressure cycle into account. **Figure 5a** shows the permeating flux interpolated at 100 mbar transassembly pressure. The corresponding assemblies are visualized in the micrographs in **Figure 5d,e**. In some cases, few particles were printed onto the glass due to a slight deviation angle between microfluidic chip and printing plane direction (**Figure 5e2**). If these fixed particles were preliminary outside the particle assembly area, the experiment was counted, decreasing the initial particle count for the hydraulic resistance calculation.

The 20 μm diameter rigid spheres show a decreasing flow with increasing particle number (**Figure 5a,d1–d3**). The 20 μm sized soft particle measurement (**Figure 5d4**) uncovers that the particle material's softness and deformability influences the hydraulic resistance significantly. The same amount of

soft particles results in a fourfold hydraulic resistance compared to the same sized rigid particles. (**Figure 5c**) Transferring the filtrate flux equation (1) for membrane processes^[36] to the hydraulic resistance of an assembly gives an estimate about the relationship between particle mass and hydraulic resistance. The equation goes

$$J = \frac{\Delta p}{\mu(R_m + \alpha \cdot m)} \quad (1)$$

while J is the permeating flux, Δp the transassembly pressure, μ the fluid viscosity, R_m the filter structure resistance, α the specific assembly resistance, and m the mass of the particle assembly per unit channel cross section area. Fitting this filtrate flux equation for the measured resistances for different assembly masses m (**Figure 5c**), results in a linear correlation of particle mass and hydraulic resistance. The extrapolated interception with the y -axis, R_m , indicates that the filter structure's resistance R_m has a great share of the overall hydraulic resistance. The empty channel resistances without particles were measured for six individual channels (Data in **Figure S6**, Supporting Information) and added as triangles to **Figure 5c**. The different values for rigid and soft particles result from the two working fluids, isopropanol and ethanol. The two fluids had to be used to suppress the agglomeration of the particles for the two material systems. Due to the different solvent resistances, a

precise comparison of rigid and soft particles is not reasonable. However, extrapolating the linear relationship of the particle mass suits the measured empty channel resistances and confirms the accuracy of the measurement.

We additionally calculated the assembly's particle volume fraction (Figure 5b) by dividing the real volume of the particles by the measured assembly volume obtained from the micrographs (see Experimental Section). The particle volume fraction increases for increasing particle number for rigid and soft particles, indicating a denser packing. Upon permeation, a larger assembly experiences an increased drag force toward the filter structure because the hydraulic resistance of all particle layers sums up. Accordingly, particles tend to fill up voids and rearrange in the assembly toward the filter structure as shown in the study of Lueken et al.^[33] and increase the overall volume fraction. As expected, same-sized particles made from a soft material show higher packing densities (Figure 5 d3,d4). On the one hand, the soft material deforms reversibly under flow compression. On the other hand, the softness promotes filling voids smaller than the original particle diameter, which is not accessible for rigid particles. The significantly higher hydraulic

resistance of the soft 20 μm sized particles suits the increased particle volume fraction.

2.2.4. Tailoring Pressure Loss by Particle Shape

The direct laser wiring process allows the fabrication of non-spherical 3D particles, enabling a tailored hydrodynamic resistance and packing density. This section investigates how the assembly's hydrodynamic resistance and packing density depend on the particles' shape and porosity.

Porous particles were generated by introducing 8 μm holes for the 20 μm sized rigid particles and 16 μm holes for the 40 μm sized soft particles along all three axes and analyzed in comparison to the identically sized spheres (Figure 6). Rigid and soft porous particles decrease the flow upon permeation. The porosity does not influence the volume fraction for the rigid particles, but increases strongly for the soft particles (Figure 6b). For those soft particles, the deformation (Figure 6 d3) compresses the holes and increases the volume fraction (Figure 6b). However, it must be noticed that the holes

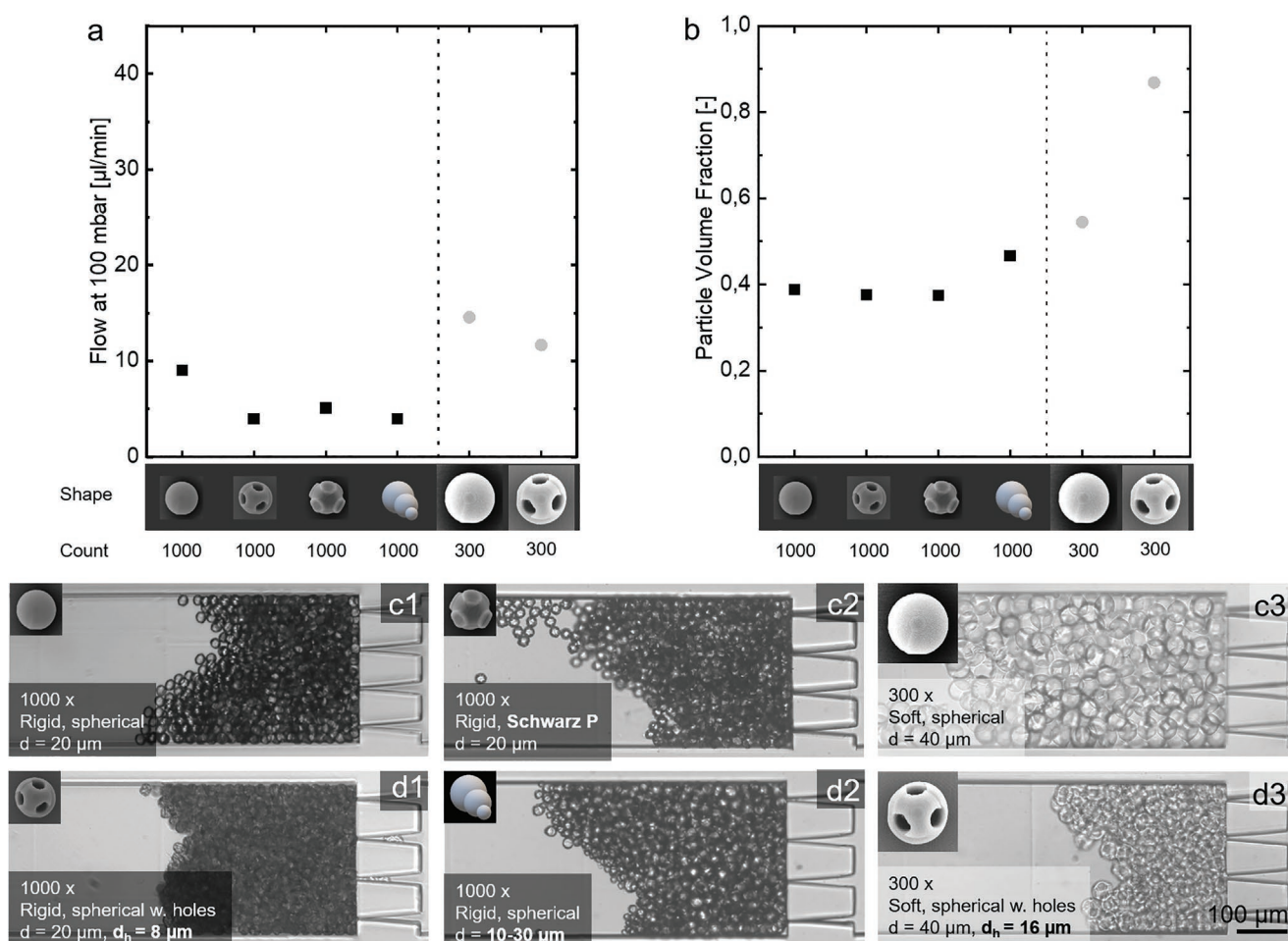


Figure 6. Influence of different particle shapes on the flow a) at 100 mbar TMP and b) volume fraction for differently shaped particles. c1) Baseline are rigid (black) 20 μm sized particles in the shape of spheres and d1) they are compared to porous spheres with 8 μm holes, c2) P-schwarz unit cell particles, and d2) 10–30 μm sized polydisperse particle mixture. Additionally, c3) soft (grey) 40 μm sized spheres are compared with d3) 40 μm sized spheres with 16 μm holes.

are not considered in calculating the particle volume. Accordingly, for the soft particles, the holes increase the compressibility of the assembly resulting in a denser packing with smaller permeable voids but does not contribute to increased permeation. The counter-intuitive permeation data of the rigid particles with holes result from the direct contact between single particles. Spherical particles contact each other at a single point, generating larger voids between the particles. The particles with holes can smoothly adapt into the ring-shaped openings of the holes from the neighboring particle. This contact reduces the distance between the particle center points and void sizes in the assembly, increasing the hydraulic resistance.^[25] Additionally, the ring-shaped contact increases attractive forces between particles and reduces particle mobility inside the assembly. On the one hand, reduced mobility supports nonuniformity and decreases the average particle volume fraction. On the other hand, the ring-shaped particle contact reduces the particle distance and increases the particle volume fraction. Although the reduced mobility and the reduced particle distance counteract the particle volume fraction, both phenomena superpose with the hydraulic resistance of the overall assembly. Therefore, they support the experimental data of a constant particle volume fraction (Figure 6b) with increased resistance (Figure 6a).

The polydisperse sample consists of 1000 particles with sizes from 10 to 30 μm (Figure S4, Supporting Information). The P-Schwarz unit-cell particles and the polydisperse sample behave similar to the porous spheres, increasing the hydraulic resistance compared to spheres. This phenomenon can also be related to an increased number of contact points reducing the average void

size inside the assembly. The increased particle volume fraction of the polydisperse sample confirms this phenomenon.

The hydraulic resistance analysis illustrates the importance of the particle shape for tailoring the pressure loss of an assembly. Smaller particles increase the surface relative to its volume, such that the influence of attractive contact forces between particles gains importance compared to larger any-shape particles. Furthermore, the 3D shape gives an additional set of design parameters, including the number of contact points and contact area to tailor attractive and repulsive particle interactions additionally to the material properties, for example, the Gibbs free energy.^[37]

2.3. Particles as Scaffolds for a Bio-Hybrid Tissue

The application of particle assemblies as scaffolds for cell tissue is advantageous due to the flexibility in processing, such as pipetting, and its ability to react to ambient conditions, such as a given reactor shape or a permeating flow. Furthermore, tuning the particle geometry can increase the surface-to-volume ratio and tailor the hydrodynamic properties of an assembly. On the next step toward showcasing such a 3D biohybrid tissue, we cultivated mouse fibroblast cells in a petri dish, which was partly covered with VFL-printed 20 μm sized spherical particles with 8 μm holes made from non-cytotoxic and low fluorescent IP-VISIO resin (Figure 7a). After four days of cultivation, we visualized the interaction of cells and particles using laser scanning confocal microscopy.

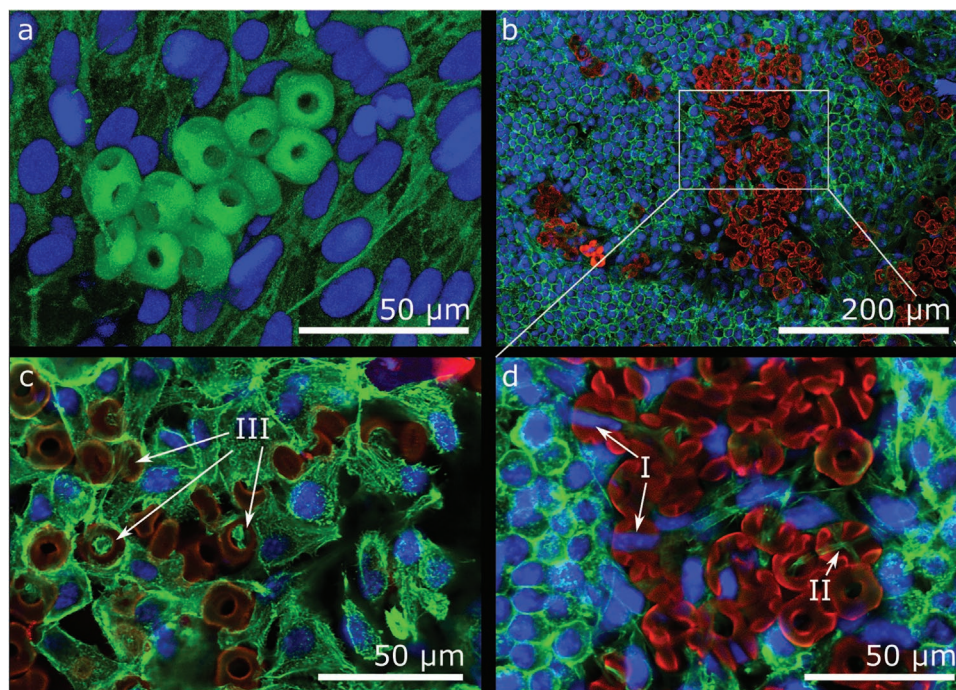


Figure 7. Confocal micrographs of VFL-fabricated 20 μm sized particles with 8 μm holes as cell culture tissue. A 3D visualization of the particles (green) in the cell-assembly is generated from a confocal z-stack image. a) The particles seem slightly deformed because of the tilted 3D z-stack visualization. Interactions of the cells and particles (red) are visualized as b) confocal micrograph in an overview and c,d) in two detailed visualizations. I) signs cell-infiltration into the porous particles, II) shows actin filament percolating porous particles, and III) displays actin filament attaching to the particle surface connecting the assembly.

Table 1. Contact angles of the applied materials with Water, Isopropanol and Ethanol as liquid phase.

Resin	IP-PDMS	IP-VISIO	IP-L
H ₂ O	108.3	70.9	66.9
Isopropanol	29.5 ^{a)}	36.4 ^{a)}	30.0 ^{a)}
Ethanol	30.7 ^{a)}	37.7 ^{a)}	32.0 ^{a)}

^{a)}The droplet quickly wetted the material, fully covering the resin sample; therefore, the first contact frame was evaluated.

IP-VISIO's zeta potential at pH7 is -44.8 ± 0.5 mV and its contact angle (Table 1) demonstrates good wettability for the particles used in cell culture experiments. In literature, contact angles of 60–80° for fibroblast cells could be determined as optimum.^[38] With a contact angle of 70.9° for water, the fabricated particles are located in the middle of the optimum range. However, in terms of protein adsorption and cell adhesion, surface wettability cannot be decoupled from other impact factors such as surface charge, surface roughness, functional chemistry or mechanical stiffness.^[39]

During cultivation, the cells spread on the surface of the well-plate and grew inside the areas where particles were located (Figure 7b). The close-up micrographs in Figure 7c,d reveal a smooth transition from areas without particles to areas with particles. The apparent darker areas in Figure 7b at the particle-covered areas are attributed to the limited field of depth of confocal imaging, fluorescent signal loss by the particles, and microbubbles attaching to the particles during cell seeding. The cells show a manifold interaction with the particles, infiltrating the porous structures of the particles (Figure 7I) and percolating and connecting various particles by the actin filament (Figure 7 II,III)

Figure 7a additionally reveals another artifact of the VFL fabrication method. Two of the visualized particles result from the start-up procedure of the VFL fabrication process, where the vertical flow was not in a steady state yet. In this specific experiment, the print was started early during this start-up procedure, squeezing the first few hundred particles in z-dimension.

This study shows manifold interactions between the particle's geometry and the cells and encourages to study further the influence of particle shape, material, and surface roughness on cell–particle interaction. Specifically, adaptations of biodegradable direct laser writing materials to VFL technology^[40–43] would open a pathway to broaden the applicability as biohybrid tissue.

2.4. Particle Agglomeration and Self-Assembly

The any-shape particles reveal different agglomeration and self-assembly tendencies, which mainly depend on two aspects. The first most prominent aspect is the wettability of the particle material by the solvent. Dissolving the particles in a nonwetting aqueous solvent supports particle agglomeration by minimizing the wetted surface. A well-wetting solvent, such as isopropanol, encourages the dispersion of single particles. Contact angle measurements prove the well-wetting behavior of the applied permeation fluids ethanol and isopropanol in Section 2.2 for IP-PDMS and IP-L, respectively. Additional contact angles

are added for completeness. The hydraulic resistance studies unravel the second aspect of particle agglomeration. Particles with larger contact areas and more contact points increase the interparticle attractive forces and promote agglomeration. The assembly compression studies confirm these observations. Compressed assemblies with increased inter-particle contact area result in more robust agglomerations withstanding the executed ultrasonic treatment.

Particularly during the cell cultivation experiments, the particles agglomerate in the well plate assembling in certain regions, while other areas do not contain any particles (Figure 7b). This inhomogeneity results from the sample preparation process. After particle fabrication and purification, the isopropanol dissolved particles are pipetted into the wellplate, spreading evenly around the whole area of the well plate. After evaporation of the isopropanol, the cells are seeded with the aqueous cell-culture medium. The aqueous solvent has a significantly higher contact angle to the IP-VISIO particle material and acts as a nonwetting solvent, promoting particle mixing and agglomeration during the initial fluid flow. The few single particles remaining in the well plate stuck to the well plate without being redispersed by the aqueous cell culture medium. This example represents a macroscopic self assembly process of any-shape micro particles triggered by solvent exchange.

3. Conclusion

This study demonstrates an in-flow two-photon direct laser writing approach for the continuous high-throughput fabrication of microscopic 3D any-shape particles for tissue engineering applications. The printing process was successfully executed to fabricate 150 000 particles in 72 h, proving continuous processibility. The hydraulic permeation properties of printed particles were analyzed by assembling particles with different amounts and shapes in microfluidic channels and measuring the hydraulic resistance by permeation. The unique microfluidic trapping method allows comparability of different particle amounts, materials, and shapes matching the filtrate flux equation. The particle shape defines the contact points of neighboring particles in an assembly and influences the hydraulic resistance significantly. Further investigations on the assemblies' structural properties and their hydraulic resistances should tackle upscaling the channel dimensions to reduce wall effects and develop permeation models for predicting the particle-dependent resistance. As a first step toward a scaffold application as biohybrid tissue, mouse fibroblast cells were cultivated on the continuously printed particles and showed manifold interactions with particle assemblies. This study illustrates the particles' tendency to assemble and agglomerate depending on the solvent and the particle shape. Combining these insights of 3D particle assembly with differently shaped particles will substantially contribute toward establishing a tailored micro-particle 3D self-assembly process in future work. For describing the assembly process for this scaled particles, the particle interactions, the solvent wettability, and the influence of the particle's shape with its specific contact points and surface needs to be accounted for. Increasing complexity, the proposed direct laser writing method will also allow a combination of differently

shaped particles to generate custom layer-by-layer scaffolds (Figure 1) with, for example, capillary size and porosity gradients. The integration of capillary gradients is a promising method^[39,44] to improve cell growth into 3D particle assemblies and is realizable with the here proposed particle fabrication method. This highlights the flexibility of the VFL technology for single any-shape particles and allows for the fabrication of “smart” scaffolds for tissue engineering applications. On this pathway toward a controlled in-flow assembly, the shape-influence on the rheology of cohesive granular media,^[45] as well as the analysis of particle orientation and of the assembly’s morphology are of major importance.

4. Experimental Section

Microfluidic Device Fabrication: The microfluidic channels for VFL as well as the hydrodynamic analyses were both fabricated as described by Lölsberg et al.^[46] A negative structure of the channel was printed onto a glass substrate (Carl Roth, 25 × 57 × 1 mm) using two-photon direct laser writing (Nanoscribe GmbH, Photonic Professional GT2) and fully polymerized using an ultraviolet light source (302 nm, 8 W). The structure was afterward molded using polydimethylsiloxane (PDMS) elastomer (Dow, SylgardTM184 Silicone Elastomer Kit) and holes were punched (Rapid-Core 1.2 mm) into the PDMS mold for tubing connection. After cleaning by ultrasonication in isopropanol (Carl Roth, 99.5%) the mold was bonded to a 170 µm thick microscopy cover slide applying an absolute oxygen pressure of 0.3 mbar at 60 W for 30 s (Diener, Zepto model 3 Plasma System).

Continuous Vertical Flow Two-photon Lithography: The continuous vertical flow channel and process was adapted from Lölsberg et al.^[21] The printing files were prepared by first constructing a 3D object of the particle (Autodesk, Inventor 2021), slicing the stl design using the Describe software (Nanoscribe, Describe 2.5.5) (solid, slicing 0.6 µm, hatching 0.3 µm), and subsequently processing the gwl file for VFL using a python script, which performs two processing steps (File S1, Supporting Information). First, the script removed all z-movements from the gwl file because the moving fluid performs the z displacement. Second, it adjusted the print-time of each layer to the same value by adding wait commands for each printing layer. Elsewise, small cross-section layers with short print times would reduce the z-height compared to large cross-section layers. The liquid resin was flushed into the channel using a syringe pump (Harvard Apparatus, PHD ULTRA) and a syringe (SGE Gas Tight, 2.5 mL) with a flowrate of 17 µL h⁻¹. The syringe was connected to the microfluidic chip using FEP tubing (Darwin Microfluidics, OD: 1/16" ID: 1/32"). The outlet tubing (Smiths Medical, fine bore polythene, OD: 1.09 mm, ID: 0.38 mm) transferred the liquid resin and solidified particles into a 1.5 mL tube (Eppendorf, 1.5 mL). The particles were printed alternating at two positions with a particle distance of 20 µm, ensuring that particles did not attach to each other (Video S2, Supporting Information). The printing process was performed with a two-photon polymerization printing device (Nanoscribe GmbH, Photonic Professional GT2) applying a 25× objective, a scan speed of 65 000 µm s⁻¹, and a laser power of 100% (50 mW minus optical losses). The harvested sample was developed and separated from the liquid resist by dilution, centrifugation, and subsequently pipetting the supernatant. This procedure was repeated three times using 1-methoxy-2-propyl-acetate (Sigma Aldrich, 99%) (10.000 s⁻¹, 10 min) and six times using isopropanol (Sigma Aldrich, 99%) (5.000 s⁻¹, 5 min).

In-Channel Particle Fabrication: The hydraulic resistances of the assemblies were measured by printing the particles inside a microchannel inside the analysis domain with two filter structures having a size of H/W/L of 100/300/3000 µm. The microfluidic PDMS channel was manually filled with the photoresist (IP L or IP PDMS, Nanoscribe GmbH) using a syringe and then placed in the two-photon printer (Nanoscribe GmbH, Photonic Professional GT2) in

oil-immersion mode using a 25× objective. The resist was given 30 min to rest to avoid currents caused by the filling. The particles were sliced using the Describe software (solid, slicing 0.6 µm, hatching 0.3 µm) and printed (scan speed 65 000 µm s⁻¹, laser power 100%, z-direction downward) as an array with a distance of 25 µm away from the membrane structure (Figure 3). (Video S3, Supporting Information) The filtration experiments were prepared by removing the liquid photoresist by flushing solvent through the channel using a constant pressure pump (Elveflow, OBI Mk3+). First, tubing and channels were filled with the new solvent by flushing from inlet 1 to outlet 1 and inlet 2 to outlet 2. Afterward, both outlets were closed, and the solvent was flushed from inlet 1 to inlet 2. The rigid IP L particles were developed using first Acetonitrile and afterward Isopropanol as filtration fluid. The soft IP PDMS particles were developed using ethanol as a developer and as a working fluid. The Young’s Modulus of the materials was taken from the material’s datasheet.

Hydrodynamic Permeation Experiments: A reservoir containing the working fluid was connected to the constant pressure pump. In between the reservoir and the microfluidic chip two flow sensors (Bronkhorst Coriolis Flow Rate Sensor, Elveflow, Microfluidic Flow Rate Sensor MFS2, Elveflow) and a pressure sensor (Microfluidic Pressure Sensor MPS1, Elveflow) were installed and connected via FEP tubing. All flow data presented in this study were measured using the MFS2 sensor. The outlet channel of the chip was connected to a waste reservoir. During filtration experiments, the assembly was situated on an optical light microscope (Leica DM IL LED, 10× objective) and recorded using Basler Video Recording Software. The filtration experiments were conducted immediately after the development using isopropanol (IP L) and ethanol (IP PDMS) as the working fluids. For this purpose, the two outlets were closed, and the pressure was set to 50 mbar. After particles accumulation at the filter structure, the pressure controller was increased to 200 mbar, resulting in a TMP of ≈150 mbar and reduced step-wise in 30 mbar steps. This procedure was called a filtration cycle. After each permeation cycle, the assembly was backflushed and sonicated for 5 min (Elmasonic xtra TT) to redisperse the particles. The filtration cycle was repeated three times for each experiment. The pressure and flow data for each pressure step were obtained by taking the average from the last 10 s corresponding to 19 data points. Additionally, a corresponding image was taken from the assembly. In some cases, several particles were printed onto the glass due to a slight deviation angle between microfluidic chip and printing plane direction. In this case, the stuck particles were not counted and not considered for hydraulic resistance calculation.

Particle Volume Fraction: The particle volume fraction was calculated with

$$\phi_p = \frac{V_{p,\text{total}}}{A_{\text{As}} \cdot h_c} \quad (2)$$

where ϕ_p is the particle volume fraction at the highest pressure step, $V_{p,\text{total}}$ the total volume of all particles in the assembly, A_{As} the x/y area of the assembly, and h_c the height of the channel (100 µm). A_{As} was manually measured for all filtration experiments from microscopic images of the respective first filtration cycle at the highest pressure step using ImageJ. The total particle volume of the spheres with holes was calculated without considering the holes.

Cell Culture: The interaction of particles with L929 mouse fibroblast cells was investigated in self built PDMS wells. PDMS and crosslinker (Dow, SylgardTM184 Silicone Elastomer Kit) were poured in a petri dish in a ratio of 10:1 and were cured at 60 °C overnight. Subsequently, a PDMS slab was cut out from the petri dish, and wells were integrated using a 4 mm biopsy puncher (EMS, Rapid-Core 4.00 mm). The PDMS slab was then plasma bonded to a microscopy cover slide applying an absolute oxygen pressure of 0.3 mbar at 60 W for 30 s (Diener, Zepto model 3 Plasma System). Finally, the PDMS wellplate was sterilized at 121 °C for 20 min (SystecTM VX-95). 20 µm sized spherical particles with 8 µm holes were printed using continuous VFL using IP-VISIO resist, which was noncytotoxic according to ISO 10993-5/ USP 87 (Nanoscribe

GmbH & Co. KG). The low auto-fluorescence of the IP-VISIO resist was advantageous for laser-based imaging applications. Particles suspended in isopropanol (Sigma Aldrich, 99%) were added to the wells and the isopropanol was evaporated at room temperature under sterile conditions. Subsequently, the wellplates were washed multiple times with sterile MilliQ water. Finally, they were incubated overnight in Roswell Park Memorial Institute (RPMI) 1640 medium (4500 mg L⁻¹ glucose, L-glutamine, sodium pyruvate, sodium bicarbonate) supplemented with 10% v/v fetal bovine serum and 1% v/v penicillin streptomycin. Cells were seeded at a concentration of 10000 cells per well. After 4 days of cultivation, the cells were fixed in 4% v/v paraformaldehyde (PFA) for 15 min, permeabilized in a 0.1% v/v Triton X-100 solution for 15 min and rinsed thoroughly in phosphate-buffered saline (PBS 1x). For the analysis of cell-particle interactions, the cells were stained for nuclei and F-actin by exposing the specimen to DAPI solution (Abcam, UK) for 5 min and Phalloidin-iFluor 488 reagent (Abcam, United Kingdom) for 120 min. Finally, the samples were imaged using a TCS SP8 Falcon confocal microscope (Leica, Germany).

Analysis of Material Properties: Contact wetting angle of the materials were measured using SurPass 3 (Anton Paar). The zeta potential of the IP-VISIO material was measured at pH7 using DSA10 (Krüss) by calculating an average value standard deviation from five measurements.

Supporting Information

Supporting Information is available from the Wiley Online Library or from the author.

Acknowledgements

A.L. and L.S. contributed equally to this work. The authors wish to acknowledge support via the Deutsche Forschungsgemeinschaft through the collaborative research center SFB 985 "Functional microgels and microgel systems." M.W. acknowledges DFG funding through the Gottfried Wilhelm Leibniz Award 2019 (WE 4678/12-1). Part of the work was performed at the Center for Chemical Polymer Technology CPT, which is supported by the EU and the federal state of North Rhine-Westphalia (grant no. EFRE 300 088 302). The authors thank Karin Faensen for capturing SEM images, Timo Linzenmeier for analyzing material properties, Matthias Geiger, and Jonas Lölsberg for early stage research and fruitful discussions, and Alexander Limper for his support in image rendering.

Open access funding enabled and organized by Projekt DEAL.

Conflict of Interest

The authors declare no conflict of interest.

Data Availability Statement

The data that support the findings of this study are available from the corresponding author upon reasonable request.

Keywords

building blocks, cohesive granular media, direct laser writing, flow assembly, permeability, tissue engineering, vertical flow fabrication

Received: December 3, 2021

Revised: January 30, 2022

Published online: March 4, 2022

- [1] B. Kiss, U. Gottschalk, M. Pohlscheidt, *New Bioprocessing Strategies: Development and Manufacturing of Recombinant Antibodies and Proteins*, Springer, Cham **2018**.
- [2] P. G. Antolli, Z. Liu, *Bioreactors: Design, Properties, and Applications, Biochemistry Research Trends*, NOVA/Nova Science Publishers, New York **2012**.
- [3] J. M. Piret, C. L. Cooney, *Biotechnol. Adv.* **1990**, *8*, 4.
- [4] H. Eghbali, M. M. Nava, D. Mohebbi-Kalhari, M. T. Raimondi, *Int. J. Artif. Organs* **2016**, *39*, 1.
- [5] F. Meuwly, P.-A. Ruffieux, A. Kadouri, U. von Stockar, *Biotechnol. Adv.* **2007**, *25*, 45.
- [6] S. B. Rauer, D. J. Bell, P. Jain, K. Rahimi, D. Felder, J. Linkhorst, M. Wessling, *Adv. Mater. Technol.* **2021**, *2*, 2100836.
- [7] A. D. Dias, J. M. Elicson, W. L. Murphy, *Adv. Healthcare Mater.* **2017**, *6*, 16.
- [8] K. M. Brunner, H. D. Perez, R. P. S. Peguin, J. C. Duncan, L. D. Harrison, C. H. Bartholomew, W. C. Hecker, *Ind. Eng. Chem. Res.* **2015**, *54*, 2902.
- [9] S. Flaischlen, G. D. Wehinger, *ChemEngineering* **2019**, *3*, 52.
- [10] M. Klumpp, A. Inayat, J. Schwerdtfeger, C. Körner, R. F. Singer, H. Freund, W. Schwieger, *Chem. Eng. J.* **2014**, *242*, 364.
- [11] M. Lämmermann, G. Horak, W. Schwieger, H. Freund, *Chem. Eng. Process.—Process Intensif.* **2018**, *126*, 178.
- [12] J. P. Rolland, B. W. Maynor, L. E. Euliss, A. E. Exner, G. M. Denison, J. M. DeSimone, *J. Am. Chem. Soc.* **2005**, *127*, 10096.
- [13] J. C. Rose, M. Cámara-Torres, K. Rahimi, J. Köhler, M. Möller, L. de Laporte, *Nano Lett.* **2017**, *17*, 3782.
- [14] R. P. Doherty, T. Varkevisser, M. Teunisse, J. Hoeft, S. Ketzetzi, S. Ouhajji, D. J. Kraft, *Soft Matter* **2020**, *16*, 10463.
- [15] A. J. D. Krüger, O. Bakirman, L. P. B. Guerzoni, A. Jans, D. B. Gehlen, D. Rommel, T. Haraszti, A. J. C. Kuehne, L. de Laporte, *Adv. Mater.* **2019**, *31*, e1903668.
- [16] D. Dendukuri, D. C. Pregibon, J. Collins, T. A. Hatton, P. S. Doyle, *Nat. Mater.* **2006**, *5*, 365.
- [17] H. J. M. Wolff, J. Linkhorst, T. Göttlich, J. Savinsky, A. J. D. Krüger, L. de Laporte, M. Wessling, *Lab Chip* **2020**, *20*, 285.
- [18] D. Dendukuri, S. S. Gu, D. C. Pregibon, T. A. Hatton, P. S. Doyle, *Lab Chip* **2007**, *7*, 818.
- [19] L. A. Shaw, S. Chizari, M. Shusteff, H. Naghsh-Nilchi, D. Di Carlo, J. B. Hopkins, *Opt. Express* **2018**, *26*, 13543.
- [20] S. Habasaki, W. C. Lee, S. Yoshida, S. Takeuchi, *Small* **2015**, *11*, 6391.
- [21] J. Lölsberg, A. Cinar, D. Felder, G. Linz, S. Djeljadini, M. Wessling, *Small* **2019**, *15*, e1901356.
- [22] I. Bouhid de Aguiar, T. van de Laar, M. Meireles, A. Bouchoux, J. Sprakel, K. Schroën, *Sci. Rep.* **2017**, *7*, 10223.
- [23] H. M. Wyss, E. V. Tervoort, L. J. Gauckler, *J. Am. Ceram. Soc.* **2005**, *88*, 2337.
- [24] J. Linkhorst, T. Beckmann, D. Go, A. J. C. Kuehne, M. Wessling, *Sci. Rep.* **2016**, *6*, 22376.
- [25] J. Linkhorst, J. Rabe, L. T. Hirschwald, A. J. C. Kuehne, M. Wessling, *Sci. Rep.* **2019**, *9*, 18998.
- [26] M. Niederberger, *Adv. Funct. Mater.* **2017**, *27*, 1703647.
- [27] M. Antonietti, M. Niederberger, B. Smarsly, *Dalton Trans.* **2008**, *1*, 18.
- [28] K. Zhang, M. Jiang, D. Chen, *Prog. Polym. Sci.* **2012**, *37*, 445.
- [29] D. Wang, M. Hermes, R. Kotni, Y. Wu, N. Tasios, Y. Liu, B. de Nijs, E. B. van der Wee, C. B. Murray, M. Dijkstra, A. van Blaaderen, *Nat. Commun.* **2018**, *9*, 2228.
- [30] J. J. Richardson, J. Cui, M. Björnmalin, J. A. Braunger, H. Ejima, F. Caruso, *Chem. Rev.* **2016**, *116*, 14828.
- [31] J. Bauer, A. Guell Izard, Y. Zhang, T. Baldacchini, L. Valdevit, *Adv. Mater. Technol.* **2019**, *4*, 1900146.
- [32] L. J. Jiang, Y. S. Zhou, W. Xiong, Y. Gao, X. Huang, L. Jiang, T. Baldacchini, J.-F. Silvain, Y. F. Lu, *Opt. Lett.* **2014**, *39*, 3034.
- [33] A. Lüken, L. Stüwe, J. Lohaus, J. Linkhorst, M. Wessling, *Sci. Rep.* **2021**, *11*, 12836.

- [34] M. Jafari, N. Derlon, P. Desmond, M. C. M. van Loosdrecht, E. Morgenroth, C. Picioreanu, *Water Res.* **2019**, *157*, 335.
- [35] S. Kerdi, A. Qamar, A. Alpatova, N. Ghaffour, *J. Membr. Sci.* **2019**, *583*, 81.
- [36] R. Rautenbach, T. Melin, *Membranverfahren*, Springer, Berlin **2004**.
- [37] F. Zamani, A. Ullah, E. Akhondi, H. J. Tanudjaja, E. R. Cornelissen, A. Honciuc, A. G. Fane, J. W. Chew, *J. Membr. Sci.* **2016**, *510*, 101.
- [38] S. Cai, C. Wu, W. Yang, W. Liang, H. Yu, L. Liu, *Nanotechnol. Rev.* **2020**, *9*, 971.
- [39] M. Ferrari, F. Cirisano, M. C. Morán, *Colloids Interfaces* **2019**, *3*, 48.
- [40] R. M. Felfel, L. Poocha, M. Gimeno-Fabra, T. Milde, G. Hildebrand, I. Ahmed, C. Scotchford, V. Sottile, D. M. Grant, K. Liefeth, *Biomed. Mater.* **2016**, *11*, 015011.
- [41] E. Kämpylä, T. Sedláčik, D. B. Aydogan, J. Viitanen, F. Rypáček, M. Kellomäki, *Mater. Sci. Eng. C, Mater. Biol. Appl.* **2014**, *43*, 280.
- [42] J. Torgersen, A. Ovsianikov, V. Mironov, N. Pucher, X. Qin, Z. Li, K. Cicha, T. Machacek, R. Liska, V. Jantsch, J. Stampfl, *J. Biomed. Opt.* **2012**, *17*, 105008.
- [43] J. Xing, L. Liu, X. Song, Y. Zhao, L. Zhang, X. Dong, F. Jin, M. Zheng, X. Duan, *J. Mater. Chem. B* **2015**, *3*, 8486.
- [44] H. Bai, D. Wang, B. Delattre, W. Gao, J. De Coninck, S. Li, A. P. Tomsia, *Acta Biomater.* **2015**, *20*, 113.
- [45] S. Mandal, M. Nicolas, O. Pouliquen, *Proc. Natl. Acad. Sci. U. S. A.* **2020**, *117*, 8366.
- [46] J. Lölsberg, J. Linkhorst, A. Cinar, A. Jans, A. J. C. Kuehne, M. Wessling, *Lab Chip* **2018**, *18*, 1341.